Article

Structural Screening and Design of Pt-nanosamples for Oxygen Reduction

Kevin Rossi, Gian Giacomo Asara, and Francesca Baletto

ACS Catal., **Just Accepted Manuscript** • DOI: 10.1021/acscatal.9b05202 • Publication Date (Web): 24 Feb 2020

Structural Screening and Design of Pt-nanosamples for Oxygen Reduction

Kevin Rossi,[†,‡] Gian Giacomo Asara,[†] and Francesca Baletto[*,†]

†*Physics Department, King's College London, Strand, WC2R 2LS, UK*

‡*Laboratory of Computational Science and Modeling (COSMO), Institute of materials, Ecole Polytechnique Fédérale de Lausanne (EPFL), Lausanne, 1015, Switzerland*

E-mail: *francesca.baletto@kcl.ac.uk

Abstract

Nanocatalysts by design promise to empower the next generation of electrodes for energy devices. However, current numerical methods deal with individual and often geometrical closed-shell nanoparticles, neglecting how the coexistence of several and structurally diverse isomers in a sample affect the activity of the latter. Here, we present a multiscale numerical approach to calculate in a fast and high-throughput fashion the current density and mass activity of individual isomers as well as to predict the activity of morphologically diverse but size-selected samples. We propose specific design rules of Pt-nanosamples for the electrochemical reduction of molecular oxygen, identifying the size-range up to 5.5 nm as the one where isomerisation of individual nanoparticles and the morphological composition of the sample can not be neglected. We confirm a peak of the activity of defected and concave polyhedra at 2-3 nm whilst spherical but amorphous isomers become the most active between 3-5 nm, with an astonishing mass activity of 2.7 A/mg. We provide a possible explanation to rationalize the discrepancies in the measured mass activity of size-selected samples in terms of the different distributions of Pt-isomers in each specimen.

Pt-nanoparticles, Oxygen Reduction Reaction, Computational Hydrogen Model for nanoparticles, Nanoparticle Design, Nanoparticle Genome, Heterogeneous Catalysis

Introduction

In the long pathway that brings catalysis towards a more and more predictive science, several milestones have been signed off. Since the pioneering work by Ertl,[1] we have deepened our mechanistic understanding of catalytic reactions thanks to the identification and characterisation, at the atomic level, of how and where chemical reactions occur.[2,3] This discovery process has enabled to draw valuable structure-activity relationships that, together with the screening of new catalytic materials, play a crucial role in the rational design of well-defined catalysts. The catalysis-by-design project, enabled by the constant advances in experimental and numerical tools, therefore, tackles today and future world socio-economics burdens, predicting the optimal elemental components of greener and more sustainable devices, e.g. efficient nano-engineered electrodes for fuel cells and batteries.[4–6] Metallic nanoparticles (MNPs) are an obvious choice as heterogeneous catalysts in electrochemical devices, overcoming the limitations of the chemistry of extended surfaces.[7] They offer a high surface-to-volume ratio, a reduced load of rare metal and a variety of adsorption sites with a variable coordination.[8]

Instruments and protocols for industrial scale yields of metallic nanocatalysts are at reach, with nowadays size-selected MNPs synthesized within an unprecedented accuracy and precision (mono-dispersivity), at a rate of $\sim$ 1 gram per hour.[9,10] On the other hand, the production of optimal nanocatalysts is possibly lagging behind. Despite numerous studies attempted to provide an atomistic understanding of oxygen reduction reaction (ORR), the performances and costs enabling the industrial use of Pt-MNPs based electrodes in fuel cells is still to be improved.[11] Although we witnessed Pt-based nanosamples with a mass activity above the 2017-DOE target of 0.44A/mg,,[12–14] the slow advancements in nanocatalysts'

application could rely on the non trivial identification of which structural features enhance the catalytic activity of MNPs, besides the advances of microscopy techniques in detecting geometries at the nanoscale.[15,16] On the other hand, the dependence of the catalytic activity of MNPs on their size has been widely demonstrated,[17–24]

Especially in physically grown samples, the balance of strain and surface energy contributions, the kinetics of the formation process, and thermally activated structural rearrangements lead to the coexistence of various isomers at finite temperature[15,25–29] - often also referred to as fluxionality.[30,31] Therefore, to move towards more efficient and cleaner industrial processes, new numerical approaches which deal with the fluxionality of metallic nanocatalysts, eventually suggesting routes for their synthesis, and the structural diversity of samples, are in high demand.

In the first part of this work, we present a multiscale numerical scheme to account for and disentangle the contributions from the non equivalent adsorption sites characteristic of each isomer, and to elucidate how morphological diversity in specimens affects their activity. Our model monitors the dynamical evolution of a geometrical descriptor, which uniquely identifies, classifies, and counts each adsorption sites and simultaneously provides a robust structure-property relationship. Doing so, we overcome common but eventually drastic assumptions such as considering a MNP as (i) a static object, with (ii) a FCC bulk-like core, and (iii) a surface with an ensemble of isolated and well-defined facets. To elucidate the dependence of the catalytic activity on the morphological diversity of samples, we refer to the sample-isomer-distribution (SID), i.e. the occurrence of certain isomers in the sample. This turns to be a powerful tool for a fast screening of better nanocatalysts and also a measurable quantity from, e.g. high-angle annular dark field scanning TEM,[32] trapped ion electron diffraction,[7,33] and multiple photon dissociation spectroscopy.[34,35]

Following the method description, we apply our multiscale method to screen the activity of samples of Pt-nanoparticles for oxygen reduction over a size range between 1.5-7.5 nm. We analyse the mass and specific activity of closed-shell geometries as well as highly-defected

and amorphous isomers obtained from annealing of liquid nanodroplets. We observe that the most active Pt-NPs are concave and defected polyhedra of 2-3 nm and, far more surprisingly, spherical but amorphous isomers of 3-5 nm. The latter display an average mass activity up to four-fold the one currently measured in experiments and a much greater one with respect to any closed-shell counterpart. At sizes larger than 5 nm, the shape factor seems to wane. Finally, we propose a possible explanation to the discrepancies in measured catalytic behaviours of Pt-samples for ORR based on the different isomer distribution within the samples. Our result shifts the paradigm of nanocatalyst design from controlling individual nanoarchitectures towards monitoring their ensemble statistics.

Methodology

The core assumption of the multiscale model here developed, named NanoCHE, is that the reaction free energy ΔG of the rate limiting step of the considered reaction can be written as a function of a geometrical descriptor, $\mathcal{GD}$. The $\mathcal{GD}$ should simultaneously (i) distinguish and classify uniquely every non-equivalent adsorption sites of any isomer; (ii) count their occurrence; (iii) and relate the energetics of the adsorbate to the local atomic environment of the site. In analogy with genetics, each $\mathcal{GD}$-value, α, becomes a *gene*, and the collection of all these genes constitutes the MNP's geometrical fingerprint, $\mathcal{F}_{\text{isomer}}$. The nanoparticle genome is in turn the full catalogue of the adsorption sites together with their *occurrence*, Ω, and it reflects the changes in the nature and distribution of adsorption sites.[36]

As widely demonstrated,[37,38] the atop generalised coordination number,

$$aGCN(i) = \sum_{j \in i-\text{neighbours}} CN(j)/CN_{max} \tag{1}$$

where $CN_{max} = 12$ is the maximum coordination for an atom in a FCC-bulk, can be employed as geometrical descriptor for both oxygen and CO_2 electrochemical reduction.[39,40]

Thanks to the discrete nature of the geometrical genome, the cathodic mass or specific

activity associated to the MNP's architecture can be estimated with respect to standard conditions. Indeed, at the applied potential U and temperature T, an isomer characterised by a GCN-fingerprint $\mathcal{F}_{\text{isomer}}$ produces a current density from a reaction step associated to a free reaction energy ΔG given by

$$j_{\text{isomer}}(t,T,U) \quad = \sum_{\alpha \in \mathcal{F}_{\text{isomer}}} \mathcal{C}\xi(t,T)\alpha e^{\beta \Delta G} \quad , \tag{2}$$

where all the contributions from available sites are included. A similar formalism was introduced by Tripkovic et al. where ΔG was calculated within a density functional theory approach, for adsorption sites available on low-Miller indexes surfaces.[41] In Eq. 2, β is the Maxwell-Boltzmann factor, and $\xi(t,T) = \frac{\Omega(\alpha)}{N_{\text{site}}(t,T)}$ is the relative occurrence of non-equivalent adsorption sites with respect to the total number of sites available, N_{site}, for the isomer under consideration. The prefactor $\mathcal{C}$ is fitted to reproduce the known specific current of low-Miller index surfaces. The free reaction energy of the reaction step $\Delta G = \Delta G(\alpha, U)$ depends on the geometrical descriptor value α in the fingerprint and on the applied potential U. Let us here remark again that the $\mathcal{F}_{\text{isomer}}$ is sensible to the geometry of the nanoparticle and hence it changes in correspondence of structural rearrangements and phase transitions.[36]

In agreement with the approach used in the computational hydrogen electrode model,[42,43] the applied voltage is included as an *a-posteriori* correction of the reaction free energy. ΔG is first written in terms of the $\mathcal{GD}$ descriptor and calculated in the absence of any electrochemical potential, and then an extra term that depends on the number n of electrons involved in that step of the reaction times the applied potential is added. The specific activity of an individual isomer, $\text{SA}^*_{\text{isomer}}$ in mA/cm^2, is calculated directly from Eq. 2 substituting a certain value to the applied potential U^*. By definition, the mass activity of an isomer, MA^*_{isomer}, is

$$MA^*_{\text{isomer}} = \frac{\text{SA}^*_{\text{isomer}} \text{A}_{\text{isomer}}}{M_{\text{isomer}}} \quad , \tag{3}$$

where the mass M_{isomer} of an isomer equals the number of atoms in the nanoparticle times

their atomic mass, i.e. 195 a.u. for Pt, while the MNP's area is assumed to be quantifiable as a function of the geometrical descriptor too. Considering atoms as spheres, the surface area of an isomer, A_{isomer}, can be expressed in terms of the atop generalised coordination,

$$A_{\text{isomer}} = \sum_{i=1}^{N} 4\pi r_{at}^2 (1 - aGCN(i)/12) \quad , \tag{4}$$

where the sum is over all the atoms i in the nanoparticle. Within this approximation, the surface contribution from each atom is greater for low coordinated atoms than for highly coordinated ones, as expected from a geometric argument. In Supporting Information, we compare values arising from the area calculations from the formalism introduced by Tripkovic et. al,[41] and in the approximation of spherical MNPs (see Table S2-S7 columns 5,6,7).

On top of mass activity and specific activity, we find convenient to introduce another quantity to fast screen more active isomers. In the following, we refer to the lowest theoretical over-potential, η_1, calculated as the equilibrium potential minus the potential required to produce a current density of 1 mA/cm^2, to quantify the activity of individual isomer. The lower the over-potential η_1 is, the more active the isomer for that reaction.

In the assumption that sintering and coalescence of MNPs in the specimen are negligible, each isomer contributes fully to the specific current density of the sample and hence the catalytic activity of the specimen can be expressed as the sum over individual contributions weighted by their relative abundance, $w_{\text{isomer}}(t, T)$,

$$j_{\text{sample}}(t, T, U) \quad = \quad \sum_{\text{isomer}} j_{\text{isomer}}(t, T, U) w_{\text{isomer}}(t, T) \quad , \tag{5}$$

where j_{isomer} is from Eq.5. The collection of each w_{isomer} provides the sample-isomer-distribution,

SID. Similarly the mass activity of a sample at a certain applied potential U^* is

$$MA^*_{\text{sample}}(t,T) = \sum_{\text{isomer}} MA^*_{\text{isomer}} w_{\text{isomer}}(t,T) \quad (6)$$

$$= \sum_{\text{isomer}} \text{SA}^*_{\text{isomer}}(t,T) w_{\text{isomer}}(t,T) \frac{A_{\text{isomer}}(t,T)}{M_{\text{isomer}}} \quad , \quad (7)$$

where the meaning of symbols is the same as in Eq.3.

Here, we select the generalised coordination number as the geometrical descriptor for oxygen reduction reaction catalysed by Pt nanoparticles. However, we would like to remark that NanoCHE is fully general and transferable to other systems and reactions, whenever a geometrical descriptor(s) depicts the most relevant chemical information, as for CO_2 on Cu nanoparticles.[44] The extension of our method to bi- and multi- metallic systems can be also pursued, under the condition that the chosen geometrical descriptor captures the complexity inherent to reactions on adsorption sites surrounded by atoms of different chemical species.[45] Surrogate electronic structure descriptors which are fast to compute and able to catalogue not-equivalent adsorption sites,[46] can also be employed as descriptors in Eq. 2 with good success. Machine learning predictions of adsorption energies, and hence ΔG, using an ensemble of features instead of a single geometrical descriptor are also very promising.[47,48] For supported nanoparticles, descriptor-activity relationships should be thoroughly addressed, eventually disregarding those sites in direct contact with the support.[37,49]

Setting the NanoCHE for ORR

With a focus on Pt-NPs for ORR, beyond the complexity of the process with several intermediates (O, OOH, OH, H_2O_2), the non-trivial pH- and potential-dependent reaction network,[50] the accepted rate-limiting step of ORR at the cathode in fuel cells is the proton/electron transfer to the adsorbed OH, $OH^* + H^+ + e^- \rightarrow H_2O$, for both dissociative and associative mechanisms[51] and several non equivalent sites. We assume this holds for all the type of adsorption sites on nanoparticles, regardless of their size and shape. In terms of the

atop generalised coordination number, with α spanning over the entire fingerprint,[37,38] the reaction free energy of the OH* reduction,

$$\begin{aligned} \Delta G_{\mathrm{OH}} &= -0.715 + 0.192\ \alpha \qquad \text{for } \alpha < 8.33 \\ \Delta G_{\mathrm{OH}} &= 2.483 - 0.192\ \alpha \qquad \text{for } \alpha > 8.33 \quad , \end{aligned} \tag{8}$$

holds valid also for five-fold symmetries, as shown in the Supporting Information Table S1. For the right leg of the free-energy plot, we assume a symmetrically equivalent reduction of the activity when moving from the α-value of the aGCN corresponding to the maximum activity, as in previous studies.[38] For ORR on Pt-NPs, the constant $\mathcal{C}$ in Eq.2 is set to 12.56 mA/cm^2 by fitting a linear function to the limiting specific currents of 96 mA cm^{-2} and 83 mA cm^{-2} for crystalline (111), $\alpha = 7.5$, and (100), $\alpha = 6.67$, surfaces, respectively.[43] Eq. 8 rules whether a site on Pt-NPs is more or less active for ORR. The more its coordination is closer to the top of the volcano-shaped curve, the more it is active. Fig. 1 provides a graphical representation of the structure-relationship of Eq. 8 together with snapshots of isomers, with a particular care to show examples of highly active sites. From Eq. 2 the activity of an isomer is determined by the relative amount of non-equivalent adsorption sites with a high activity, as found from their aGCN.

To forecast *on-the-fly* the correlation between catalytic activity and structural changes upon a timescale of μs, we employ an iterative temperature molecular dynamics algorithm (itMD), as available in LoDiS,[52] to monitor the evolution of the aGCN-genome, and then the mass activity during the formation process of Pt-NPs. A common neighbour analysis (CNA)[53] quantifies structural changes and defects formation, i.e. re-entrances and elongated concavities, and the formation of twin planes, grain boundaries, and five-fold axis. We thus take in consideration (5,5,5)-(4,2,2)-(4,2,1) CNA signatures.[54] itMD is a concatenation of canonical ensemble runs, each lasting a period of time $\Delta\tau$, during when the system evolves according to Newton's equation of motion (integrated by a velocity-Verlet algorithm) with

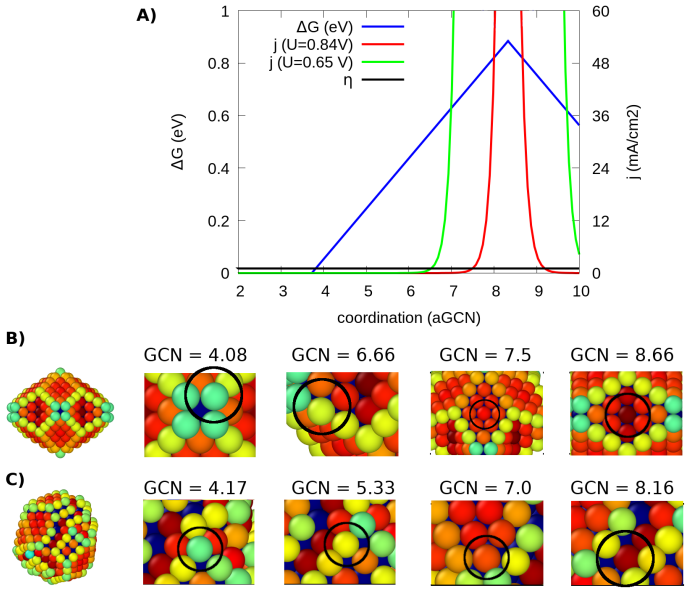

Figure 1: (A) Volcano-plot: ΔG_{OH} as a function of aGCN (blue); specific current associated to each active site from 5 assuming $\xi = 1$ at two bias values (U=0.84 V, red; and U=0.65 V, green). Below we show a MDh (B panel) and a defected twinned structure (C panel) where atoms are coloured according to their aGCN. Each snapshot highlights different adsorption sites, spanning different aGCN values. Rightmost enlargements exemplify which adsorption sites are deemed as the most active ones by the model. These correspond to adsorption sites at re-entrances, close to adatoms, or unveiled following the formation of vacancies on a surface or at facets edges.

a time step of 5 fs. The temperature, controlled by a stochastic Andersen thermostat with a frequency of 0.5 THz, is decreased by ΔT between two successive iterations, corresponding to a freezing rate of $\rho = \Delta T/\Delta\tau$.[55] The rate is chosen on the basis of the NP-size but we gather statistics from at least 8 simulations per each system. To speed-up the calculations, the second-moment approximation of the tight-binding is employed to describe the metal-metal interaction.[56]

Results and discussion

First we summarise the results obtained for individual isomers in the 1.5-7.5 nm range presenting a closed-shell geometry as well as arising from the nucleation of nanodroplets, as depicted in Figs. 2-3 and 4 respectively. We then combine those data to construct

morphological heterogeneous samples characterised by a unique SID and representative of different experimental set-ups, whose activity has been proved to be significantly different, Fig. 5.

Individual isomers

The IV-curves of the selected closed-shell isomers with a diameter of about 1.5, 3.5, 5.5 and 7.5 nm are depicted in the right panel of Fig. 2, together with snapshots for each morphology (left) and their corresponding aGCN-genome as a function of size (central).

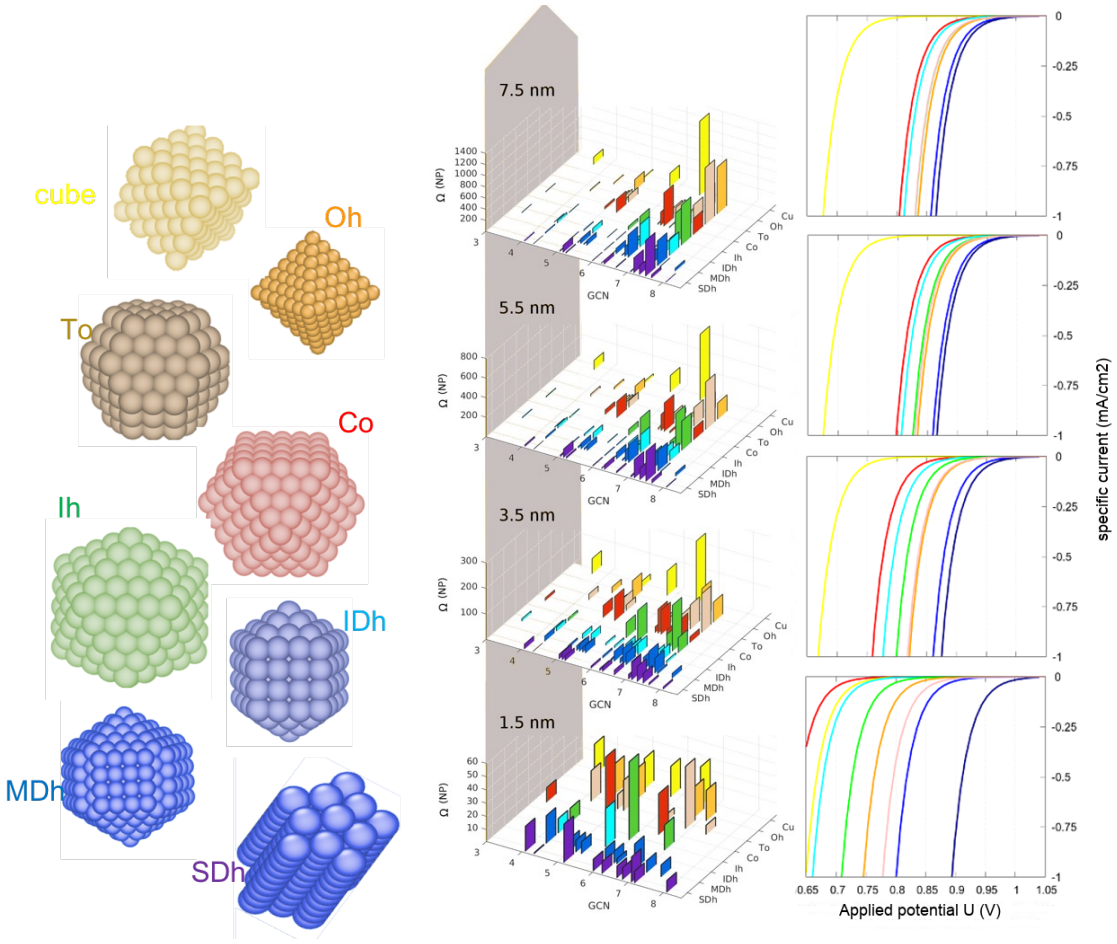

Figure 2: Closed-shell geometries snapshots, their genomic characterisation at different sizes , and their I-V curves obtained from Eq.2, are reported in the left, central, and right panel respectively. The y-axis in the I-V curves is by purpose bound at 1 mAcm^{-2} to easily estimate η_1.

The interested reader is referred to the Supporting Information Tables S2-S6 for a detailed structural and catalytic properties characterisation of each isomer taken in consideration during this screening, for a larger number of sizes, below 10 nm.

First we aim to assess the catalytic activity of individual Pt-isomers that display a well-known geometry and delimited by well-defined facets. In turn, we consider four architectures presenting a FCC geometry and delimited by (100) and/or (111) facets, namely cube (Cb), octahedron (Oh), regular truncation of an octahedron (TO), cuboctahedron (Co). Following surface energy considerations, suggesting a (111) > (100) > (110) order, twinned non-crystalline structures are likely. Among them, we examine icosahedron (Ih) and three different cuts of a pentagonal bi-pyramid: Ino-Decahedron (IDh), Marks-Decahedron (MDh), and a stellated Marks-Decahedron (SDh). The geometrical construction for such truncation is recast in terms of 3 parameters: m, n, and p, where m and n enumerate the number of atoms along the two edges of the (100) facet formed by applying cuts parallel to the five-fold axis while $p-1$ labels the number of *missing* layers in the re-entrance along the grain boundary. We select $p = 1$, $p = 2$, $p > 2$ and $m = n$, $m = n + 1$, $m = n = 2$ respectively for IDh, MDh and SDh.[25]

We note a remarkable structural effect up to 5.5 nm, with η_1 strongly varying between 0.33-0.7 V. On the other hand a negligible difference in η_1 is found when the diameter - defined as the maximum atomic pair distance - enlarges from 5.5 to 7.5 nm, with an average value of 0.41±0.02 V, excluding the two extreme and opposite cases of Cu and SDh which have a large size limit of 0.56 V and 0.37 V, respectively. For Cu, MDh and To, we register small changes of about 0.05 V in η_1 when the MNP's diameter is enlarged from 1.5 to 5.5 nm. On the other hand, in the same size range, Oh and Ih decrease their η_1 of 0.10-0.15V, while for Co and IDh the drop is even larger, 0.20 V. These changes (see also Fig. S1) are in very good agreement with recent experimental data.[22]

To stress the structural effect, Fig. 3 reports the IV-curves and the mass activity, calculated at 0.9 V, associated to each isomers. We notice that (i) the position of the maximum

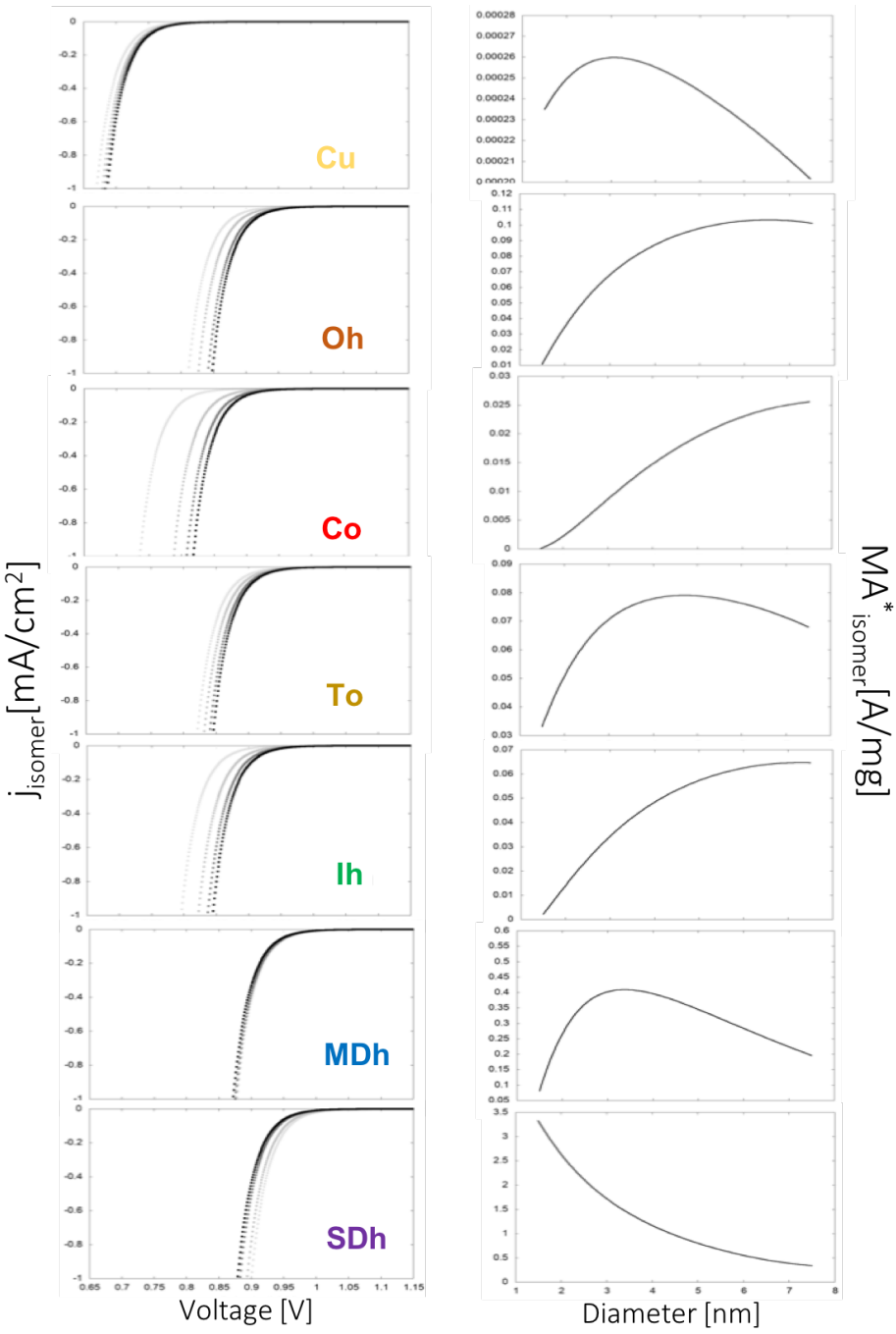

Figure 3: Homogeneous size-selected samples, at 1.5, 3.5, 5.5, 7.5 nm. Left panel: IV-curves are calculated scanning over the applied potential, as in Eq. 2, where the diameter is labelled by grey lines of increasingly dark tone. Right panel: mass activity (A/mg) is extracted at 0.9 V vs SHE using Eq. 7. The activity of homogeneous structural samples have a similar size-dependency as their individual components.

activity varies as SDh at 2 nm, Cu at 3.5 nm, Ih at 6 nm, IDh at 7 nm, while TO and Oh peaks at 3.5 and 5 nm, respectively; (ii) a drop in the activity below 1.5 nm which can be explained in terms of the aGCN-genome size-behaviour (see central panel of Fig.2). As evident from Fig. 1, the most active sites are characterised by a aGCN of 7.33-8.5. These features, with the exception for concave and elongated shapes as the SDh, are not present or scarce at small sizes, but becoming predominant above 5.5 nm (see also[36]); (iii) The maximum value of MA* spans three orders of magnitude, leading to a general trend of the activity versus the structure as SDh $\gg$ MDh $>$ Oh $\sim$ To $\sim$ Ih $\sim$ IDh $\sim$ Co $\gg$ Cu.

Nucleation of Pt-nanodroplets

As a case study to prove the importance of addressing structural changes on the activity of Pt-MNP for ORR, we investigate the annealing of MNPs with a radius in the 1.2-5.5 nm range, i.e. 147-309-561-923-1415-2057-2860-3871 atoms. In the itMD runs, we choose a nucleation rate ρ_s of 50 K/ns, with $\Delta T = 50$ K and $\Delta\tau = 1$ ns, and a twice faster rate for sizes above 561 atoms setting ΔT of 100K, because of the increased computational costs associated to study the freezing of larger systems. Besides structure sampled via freezing nanodroplets, we further consider the activity of quenched nanodroplets, whose annealing takes place over just a few fs. In this process we always obtain amorphous and spherical geometries, labelled as "Am". Regardless of their size, structures formed after nucleation are spherical with many surface defects and stacking faults. The characteristic features of isomers after nucleation are displayed in the paradigmatic snapshots in panel B of Fig. 4. The interested reader is referred to the dedicated section in the Supporting Information for a detailed report on the aGCN genome of these systems, Fig. S2-S13.

We classify the structures on the basis of their CNA signature. An isomer is labelled as FCC in absence of (5,5,5) signature (in red in Fig. 4); Ih when it has a relative high percentage of (5,5,5) and (4,2,2) signature (in green), as a Dh, a high (4,2,2), a small percentage of (5,5,5) (in blue), and eventually as Am when there is not a predominant CNA character

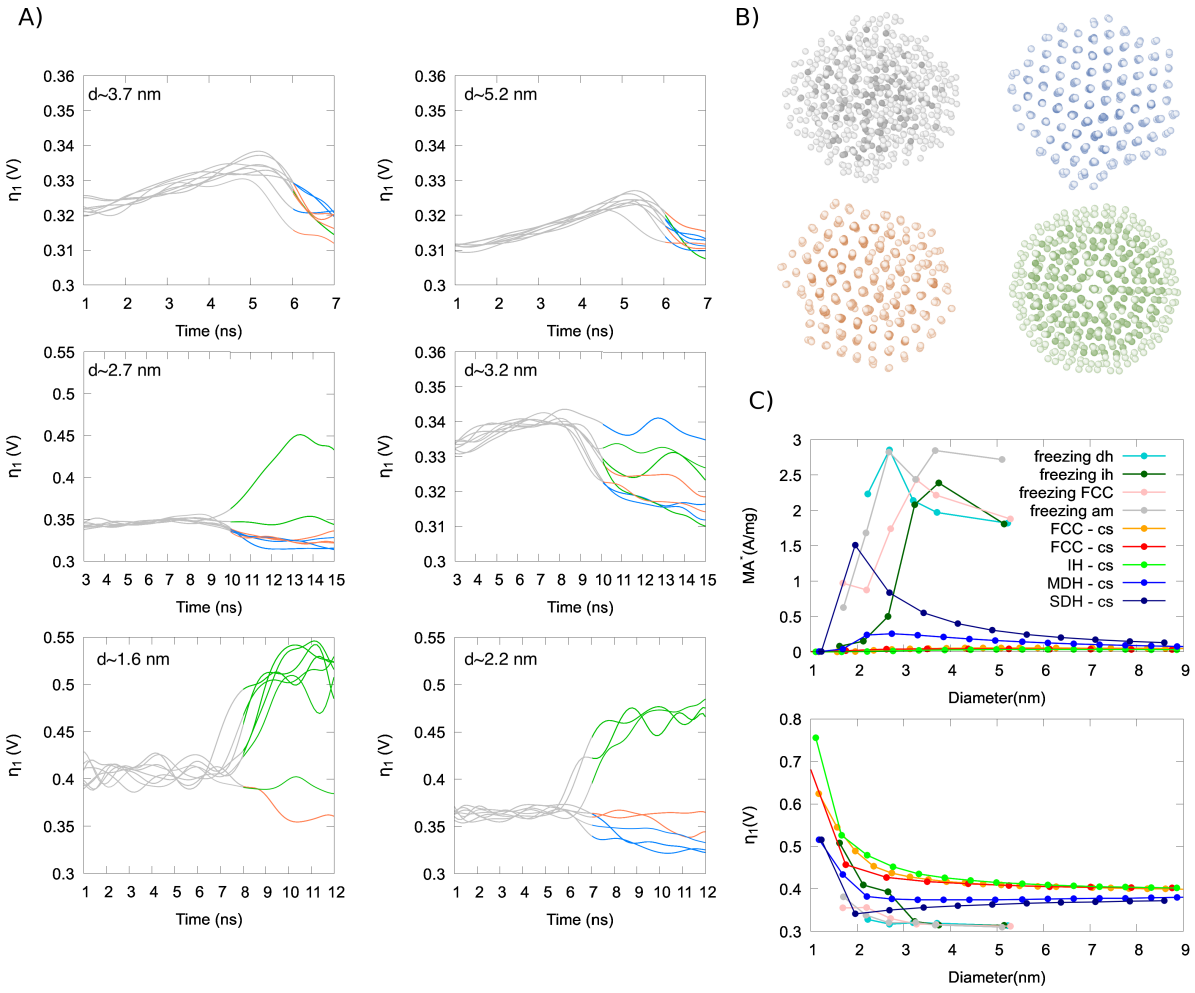

Figure 4: Panel A: η_1-evolution during annealing of Pt-nanodroplets in vacuo, at different diameters. Each line corresponds to an independent simulation. Colours refer to the structural classification of Pt-isomers into amorphous (grey); FCC (red); Dh (blue); Ih (green) families via common neighbour analysis.[53] Panel B: typical snapshots of Dh, Ih, FCC and amorphous shapes. Panel C: Comparison of η_1 and MA* between shapes obtained during annealing and their corresponding closed-shell.

(in grey). Nonetheless, the relative probability of each motif changes with size. Twinned and FCC-like isomers coexist between 2 and 5.5 nm, with Ih very frequent at small sizes but less likely above 3 nm. In specific, at 147 atoms, an Ih occurs more than 80%, and it could be both a closed-shell or an incomplete Ih. At 309, 561 and 923 atoms, all the three motifs are likely to be formed, with a probability about 25-38% for FCC and Ih, and a 38% for Dh. The Dh are usually asymmetric with an island on a HCP stacking while the FCC

contains several dislocation planes, almost parallel.[54] Perfectly closed Ih become rare, and they might nucleate with an incomplete shell. Above 1415 atoms, FCC-like are the most probable, followed closely by Dh, while the likelihood of finding Ih drops below 15%. The detailed study of how the freezing rate[57] as well as the presence of a support[37] affects the likelihood to observe one Pt-isomer or the other is a topic of great interest. This is, however, beyond the scope of the current report, and currently investigated in ongoing studies. In the following, we see what could be the effect of different isomers distribution.

Panel (A) of Fig. 4 reports η_1 evolution during the nucleation of Pt nanodroplets, while in panel (C) we plot its average per each size, together with the MA*. First, we notice that only at certain sizes and for certain morphology the activity increases after nucleation, but at the phase transition the nanoparticle might have a lower activity. Furthermore, contrasting the activities of nucleated isomers and closed-shell geometries, the former are always more active by a significant amount, stressing the importance of defects formation for ORR activity.

Table S7 (Supporting Information) reports η_1, SA* and MA* for closed-shell isomers, an average from defected polyhedra (d-poly) as obtained during the slow-nucleation and Am, as from a fast nucleation. Pt-NPs with a diameter larger than 3 nm and nucleating into defected Ih shapes have a promising activity above 1.5 A/mg. This is much higher than the MA* of their perfect close-shell counterparts. The most active isomers are defected-Dh of 2-3 nm with a MA* hitting 3 A/mg, and amorphous shapes above 3 nm. The latter present an average MA* of 2.71±0.27 A/mg. This value is three to four times larger than previously reported values in the literature.[20] The gain in MA* could be as high as twelve-fold and increases with the NP-size. Indeed, while the MA* of the best closed-shell structure peaks at small sizes just below 2 nm (147 atoms), the one of a solidified NP peaks at about 3.2 nm (923 atoms). Amorphous are better than any closed-shell isomer once the size is above 2 nm, oscillating around 2.71 ± .27 A/mg, a value significantly higher than commonly measured ones.[20] Shape effects are relevant up to 2.7 nm, where the MA* from Ih is less than one fifth of the value from Dh, and wane at 5 nm and above. Dh performed better between 2-3 nm,

while at 3-4 nm FCC-like are more active.

The analysis of isomers sampled by annealing liquid nanodroplets highlights the key importance of implementing structural disorder -i.e. defects, steps, and re-entrances at stacking faults- to enhance the nanoparticle activity. The superior activity of Am isomers is in fact due to the significant number of highly coordinated sites in the amorphous surface, in correspondence of the above listed defects (Fig. S2-S10). Further, our results show that a shape-factor is important up to 5 nm. After this size the mass activity of defected polyhedra, regardless of their specific morphology, converges to an average value of 1.83±0.03 A/mg.

Sample Isomers Distributions

We estimate the ORR mass activity of size-selected ensembles of nanoparticles which present different isomer distributions. Our aim is two-fold: (i) to characterise quantitatively the degree by which a change in the Sample-Isomer-Distribution of a specimen versus MNP size alters the profile of the mass activity; (ii) to shed light on the apparent controversy among measured data where the maximum peak of the mass activity could significantly change.[58] Besides a general consensus that the ORR mass activity peaks for Pt-nanoparticles of 2.2-3 nm in diameter, its intensity ranges from 0.1 A/mg for Shao and coworkers,[19] through 0.55 A/mg reported by Arenz et al.[18] To this end we build specimens whose SID varies with size. We consider homogeneous samples, where only one morphology is present, see Fig.3 and structurally heterogeneous sample, as reported in Fig. 5.

We then contrast the mass activity of these four specimens against sets of experimentally reported data[18,19,21,23] and report the observed trends in the right panel of Fig. 5. Although experimental set ups, e.g. linear scanning voltammetry,[59] could rationalise a different performance, we believe that the Sample-Isomer-Distribution is a fundamental quantity in the determining the catalytic activity of samples containing metallic nanoparticles. Indeed, the intensity of the activity peak and the size at which it appears can be tuned dramatically just by changing the isomer distribution.

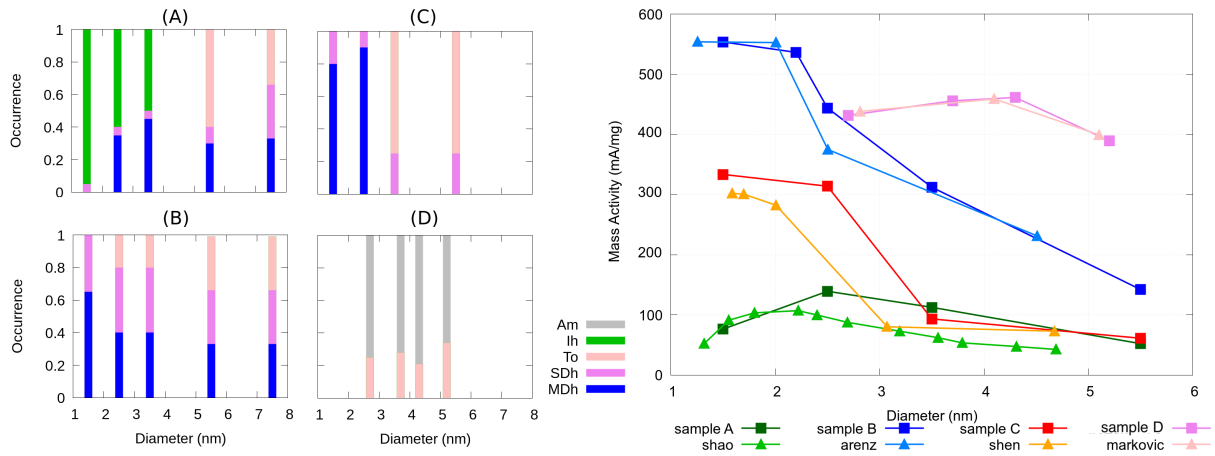

Figure 5: Activity from morphological heterogeneous samples. The morphological composition, SID, of each sample is given in the bar chart on the left, and colour coding stands for Am (grey), FCC (pink), Ih (green), SDh and MDh magenta and blue, respectively. For sake of clarity we gather FCC-like motifs with the same colour. The right hand side panel shows the comparison between the calculated mass activity (mA/mg) of the sample in triangular, and available experimental data with squared symbols. Lines are for eye-guide only. Light/Dark Green: Sample (A) - data from Ref.;[19] Orange/Red: Sample (B) - data from Ref.;[18] Light/Dark blue: Sample (C) -data from Ref.;[21] Pink/Magenta: Sample (D) -data from Ref.[23]

Rational Design Paradigms

Our results show that the rational design of nanocatalysts for oxygen reduction can follow two paradigms: one aimed at the formation of individual isomers with an abundance of highly coordinated sites, e.g. twinned structures with deep re-entrances, and isomers with a large surface disordering; the other devoted to find the formation process leading to optimal isomer distribution(s) within a size-selected sample.

Whilst at a certain thermodynamic condition, one SID should be available, the isomer distribution within an ensemble of size-selected nanoparticles can be kinetically controlled and the presence of long-life metastable structures, whose rearrangements are hindered by activation barriers much larger than the thermal energy, can not be ruled out. Although a conclusive and all-encompassing list of formation methods is well beyond the scope of this work, a general overview of common tools suggests that (i) colloidal methods can bias

favourably the formation of twinned structures with deep re-entrant facets;[28,60] (ii) aggregation sources and cluster matrix assembly can enhance kinetic trapping and disordered surfaces;[61–64] (iii) post-synthesis treatments allow to form highly coordinated sites from the removal of low coordinated ones.[12,14,59,65–67] Generally speaking, coalescence and sintering of nanoparticles lead to defected shapes with many highly coordinated surface sites and, in turn, good catalytic performances for ORR.[39,68]

Conclusions

In conclusion, we develop a new multiscale numerical method to estimate the activity of the elemental components of nano-engineered electrodes, namely metallic nanoparticles, in realistic temperature conditions. To this end we incorporate the nanoparticles genome into the computational hydrogen electrode model. To sequencing the geometrical nanoparticle genome we choose the atop generalised coordination number, but the method is general and can be used also with other geometrical descriptors. Our approach allows to establish robust design-rules of Pt-nanoparticles for oxygen reduction taking into account their fluxionality and the isomer heterogeneous distributions characteristic of experimental samples.

Among structurally well-defined nanoparticles, we confirm the high performance for oxygen reduction of Pt concave and defected polyhedra with a diameter of 2-3 nm. The analysis of Pt-nanoparticles produced by annealing shows that defected and twinned geometries are also highly active, in agreement with experimental evidence. Nonetheless, in the 3-5 nm range, spherical but amorphous Pt-isomers are the most active. These may be obtained through the fast annealing of liquid nanodroplets, and present an extraordinary average mass activity of 2.7 A/mg, about five times the actual activity of commercial Pt-nanocatalysts. we further provide a demonstration on how discrepancies in measured catalytic behaviours can be rationalised in terms of diverse morphological compositions of the samples taken for comparison.

Finally, we hope this work will pave the way to obtain feasible designs of nanoscaled metallic electrodes. Our study promotes and gives ground to a collaborative effort where numerical, characterisation (both post synthesis and in operando), and catalytic reaction data are collected, analysed and intelligently combined to rationalise the catalytic activity of nanoscaled materials for a certain reaction.

Supporting Information

This information is available free of charge on the ACS Publications website: numerical methods further details; benchmark of the GCN - ΔG scaling relationship for non-fcc cut nanoparticles; recap tables for structural and catalytic properties of closed-shell, defected, and amorphous isomers; aGCN genomes and representation of amorphous and defected isomers.

Acknowledgement

GGA and FB thank the "Towards an Understanding of Catalysis on Nanoalloys" (TOUCAN) EPSRC Critical Mass Grant (EP/J010812/1) as does KR (ER/M506357/1). All the authors are grateful to the UK Materials and Molecular Modelling Hub for computational resources, which is partially funded by EPSRC (EP/P020194/1), and to the additional financial supported offered by the Royal Society, RG 120207. GGA thanks the postdoctoral scheme offered by the NMS Faculty.

References

(1) Ertl, G. Nobel Lecture - Reactions at Surfaces: From Atoms to Complexity. www.nobelprize.org, Nobel Foundation, 2007.

(2) Prieto, G.; Schüth, F. The Yin and Yang in the Development of Catalytic Processes:

Catalysis Research and Reaction Engineering. *Ang. Chem. Int. Ed.* **2015**, *54*, 3222–3239.

(3) Catlow, C.; Davidson, M.; Hardacre, C.; Hutchings, G. Providing sustainable catalytic solutions for a rapidly changing world. *Phil. Trans. Roy. Soc. Lon. A* **2016**, *374*, 2061.

(4) Nuñez, M.; Lansford, J. L.; Vlachos, D. G. Optimization of the facet structure of transition-metal catalysts applied to the oxygen reduction reaction. *Nat. Chem.* **2019**, *11*, 449–456.

(5) Hammes-Schiffer, S. Catalysts by Design: The Power of Theory. *Acc. Chem. Res.* **2017**, *50*, 561–566.

(6) Pelletier, J.; Basset, J. Catalysis by Design: Well-Defined Single-Site Heterogeneous Catalysts. *Acc. Chem Res.* **2016**, *49(4)*, 664–77.

(7) Strasser, P.; Gliech, M.; Kuehl, S.; Moeller, T. Electrochemical processes on solid shaped nanoparticles with defined facets. *Chem. Soc. Rev.* **2018**, *47*, 715.

(8) Medford, A.; Vojvodic, A.; Hummelshøj, J.; Voss, J.; Abild-Pedersen, F.; Studt, F.; Bligaard, T.; Nilsson, A.; Nørskov, J. From the Sabatier principle to a predictive theory of transition-metal heterogeneous catalysis. *J. Catal.* **2015**, *328*, 36–42.

(9) Palmer, R. E.; Cao, L.; Yin, F. Note: Proof of principle of a new type of cluster beam source with potential for scale-up. *Rev. Sci. Instr.* **2016**, *87*, 046103.

(10) Ellis, P.; Brown, C.; Bishop, P.; Yin, J.; Cooke, K.; Terry, W.; Liu, J.; Yin, F.; Palmer, R. The cluster beam route to model catalysts and beyond. *Faraday Disc.* **2016**, *188*, 39–56.

(11) Deng, Y.; Wiberg, G.; Zana, A.; Sun, S.; Arenz, M. Tetrahexahedral Pt Nanoparticles: Comparing the Oxygen Reduction Reaction under Transient vs Steady-State Conditions. *ACS Catal.* **2017**, *7*, 1–6.

(12) Zhang, L.; Roling, L. T.; Wang, X.; Vara, M.; Chi, M.; Liu, J.; Choi, S. I.; Park, J.; Herron, J. A.; Xie, Z.; Mavrikakis, M.; Xia, Y. Platinum-based nanocages with subnanometer-thick walls and well-defined, controllable facets. *Sci.* **2015**, *349*, 412–416.

(13) Cui, C.; Gan, L.; Heggen, M.; Rudi, S.; Strasser, P. Compositional segregation in shaped Pt alloy nanoparticles and their structural behaviour during electrocatalysis. *Nat. Mat.* **2013**, *12*, 765–771.

(14) Han, B.; Carlton, C. E.; Kongkanand, A.; Kukreja, R. S.; Theobald, B. R.; Gan, L.; O'Malley, R.; Strasser, P.; Wagner, F. T.; Shao-Horn, Y. Record activity and stability of dealloyed bimetallic catalysts for proton exchange membrane fuel cells. *Ener. Env. Sci.* **2015**, *8*, 258–266.

(15) Wells, D.; Ferrando, R.; Palmer, R. Experimental determination of the energy difference between competing isomers of deposited, size-selected gold nanoclusters. *Nat. Comm.* **2018**, *9*, 1323.

(16) Pfisterer, J. H. K.; Liang, Y.; Schneider, O.; Bandarenka, A. S. Direct instrumental identification of catalytically active surface sites. *Nat.* **2017**, *549*, 74–77.

(17) Sanchez-Sanchez, C.; Solua-Gullon, J.; Vidal-Iglesias, F.; A. Aldaz, V. M.; Herrero, E. Imaging Structure Sensitive Catalysis on Different Shape-Controlled Platinum Nanoparticles. *J. Am. Chem. Soc.* **2010**, *132*, 5622–5624.

(18) Nesselberger, M.; Ashton, S.; Meier, J.; Katsounaros, I.; Mayrhofer, K.; Arenz, M. The Particle Size Effect on the Oxygen Reduction Reaction Activity of Pt Catalysts: Influence of Electrolyte and Relation to Single Crystal Models. *J. Am. Chem. Soc.* **2011**, *133*, 17428–17433.

(19) Shao, M.; Peles, A.; Shoemaker, K. Electrocatalysis on Platinum Nanoparticles: Particle Size Effect on Oxygen Reduction Reaction Activity. *Nano Let.* **2011**, *11*, 3714–3719.

(20) Perez-Alonso, F.; McCarty, D.; Niersoff, A.; Hernandez-Fernandez, P.; Strebel, C.; Stephens, I.; Nielsen, J.; Chorkendoff, I. The Effect of Size on the Oxygen Electroreduction Activity of Mass-Selected Platinum Nanoparticles. *Ang. Chem. - Int. Ed.* **2012**, *51*, 4641–4643.

(21) Sheng, W.; Chen, S.; Vescovo, E.; Shao-Horn, Y. Size Influence on the Oxygen Reduction Reaction Activity and Instability of Supported Pt Nanoparticles. *J. Elect. Soc.* **2012**, *159*, B96–B103.

(22) Anastasopoulos, A.; Davies, J.; Hannah, L.; Hayden, B.; Lee, C.; Milhano, C.; Mormiche, C.; Offin, L. The Particle Size Dependence of the Oxygen Reduction Reaction for Carbon-Supported Platinum and Palladium. *ChemSusChem* **2013**, *6*, 1973–1982.

(23) Li, D.; Wang, C.; Strmcnik, D.; Tripkovic, D.; Sun, X.; Kang, Y.; Chi, M.; Snyder, J.; Van Der Vliet, D.; Tsai, Y.; Stamenkovic, V.; Sun, S.; Markovic, N. Functional links between Pt single crystal morphology and nanoparticles with different size and shape: the oxygen reduction reaction case. *En. and Env. Sci.* **2014**, *7*, 4061–4069.

(24) Liu, Y.; Zhang, L.; Willis, B.; Mustain, W. Importance of Particle Size and Distribution in Achieving High-Activity, High-Stability Oxygen Reduction Catalysts. *ACS Cat.* **2015**, *5*, 1560–1567.

(25) Baletto, F.; Ferrando, R. Structural properties of nanoclusters: Energetic, thermodynamic, and kinetic effects. *Rev. Mod. Phys.* **2005**, *77*, 371–423.

(26) Barnard, A. Modelling of nanoparticles: Approaches to morphology and evolution. *Rep. Prog. Phys.* **2010**, *73*, 086502.

(27) Ferrando, R. Symmetry breaking and morphological instabilities in core-shell metallic nanoparticles. *J. Phys. Cond. Mat.* **2015**, *27*, 013003.

(28) Marks, L.; Peng, L. Nanoparticle shape, thermodynamics and kinetics. *J. Phys. Cond. Mat.* **2016**, *28*, 053001.

(29) Pohl, D.; Surrey, A.; Schultz, L.; Rellinghaus, B. The impact of oxygen on the morphology of gas-phase prepared Au nanoparticles. *Appl. Phys. Let.* **2012**, *101*, 263105.

(30) Hakkinen, H.; Abbet, S.; Sanchez, A.; Heiz, U.; Landman, U. Structural, electronic, and impurity-doping effects in nanoscale chemistry: supported gold nanoclusters. *Angew. Chem. Int. Ed.* **2003**, *42*, 1297–1300.

(31) Zhai, H.; Alexandrova, A. N. Fluxionality of Catalytic Clusters: When It Matters and How to Address It. *ACS Catal.* **2017**, *7*, 1905–1911.

(32) Foster, R., D.M. Ferrando; Palmer, R. Experimental determination of the energy difference between competing isomers of deposited, size-selected gold nanoclusters. *Nat. Comm.* **2018**, *9*, 1323.

(33) Rapps, T.; Ahlrichs, R.; Waldt, E.; Kappes, M. M.; Schooss, D. On the Structures of 55-Atom Transition-Metal Clusters and Their Relationship to the Crystalline Bulk. *Angew. Chem. Int. Ed.* **2013**, *52*, 6102–6105.

(34) Fielicke, A.; Meijer, G.; Von Helden, G. Infrared multiple photondissociation spectroscopy of transition metal oxide clustercations. *Eur. Phys. J. D* **2003**, *24*, 69.

(35) Harding, D.; Gruene, P.; Haertelt, M.; Meijer, G.; Fielicke, A.; Hamilton, S.; Hopkins, W.; Mackenzie, S.; Neville, S.; Walsh, T. Probing the structures of gas-phase rhodium cluster cations by far-infrared spectroscopy. *J. Chem. Phys* **2010**, *133*, 214304.

(36) Rossi, G. G., K. Asara; Baletto, F. A genomic characterisation of monometallic nanoparticles. *Phys. Chem. Chem. Phys.* **2019**, *21*, 4888–4898.

(37) Rossi, K.; Asara, G.; Baletto, F. Correlating ORR activity and structural rearrangements in MgO-supported Pt nanoparticles. *ChemPhysChem* **2019**, *20*, 3037.

(38) Rück, M.; Bandarenka, A.; Calle-Vallejo, F.; Gagliardi, A. Fast identification of optimal pure platinum nanoparticle shapes and sizes for efficient oxygen electroreduction. *Nanosc. Adv.* **2019**, *1*, 2901.

(39) Calle-Vallejo, F.; Pohl, M. D.; Reinisch, D.; Loffreda, D.; Sautet, P.; Bandarenka, A. S. Why conclusions from platinum model surfaces do not necessarily lead to enhanced nanoparticle catalysts for the oxygen reduction reaction. *Chem. Sci.* **2017**, *8*, 2283–2289.

(40) Jorgensen, M.; Grönbeck, H. Scaling Relations and Kinetic Monte Carlo Simulations To Bridge the Materials Gap in Heterogeneous Catalysis. *ACS Cat.* **2017**, *7*, 5054–5061.

(41) Tripkovic, V.; Cerri, I.; Bligaard, T.; Rossmeisl, J. The Influence of Particle Shape and Size on the Activity of Platinum Nanoparticles for Oxygen Reduction Reaction: A Density Functional Theory Study. *Cat. Let.* **2014**, *144*, 380–388.

(42) A. Kulkarni, A., S.Siahrostami; J.K.Nørskov, Understanding Catalytic Activity Trends in the Oxygen Reduction Reaction. *Chem. Rev.* **2018**, *118*, 2302–2312.

(43) Nørskov,; Rossmeisl, J.; Logadottir, J.; Lindqvist, A.; Kitchin, L.; J.R. Bligaard, T.; Jónsson, H. Origin of the Overpotential for Oxygen Reduction at a Fuel-Cell Cathode. *J. Phys. Chem. B* **2004**, *108*, 17886–17892.

(44) Zhao, Z.; Chen, Z.; Zhang, X.; Lu, G. Generalized Surface Coordination Number as an Activity Descriptor for CO2 Reduction on Cu Surfaces. *J. Phys. Chem. C* **2016**, *120*, 28125–28130.

(45) Calle-Vallejo, F.; Bandarenka, A. S. Enabling Generalized Coordination Numbers to Describe Strain Effects. *ChemSusChem* **2018**, *11*, 1824–1828.

(46) Ma, X.; Xin, H. Orbitalwise Coordination Number for Predicting Adsorption Properties of Metal Nanocatalysts. *Phys. Rev. Lett.* **2017**, *118*, 36101.

(47) Choksi, T. S.; Roling, L. T.; Streibel, V.; Abild-Pedersen, F. Predicting Adsorption Properties of Catalytic Descriptors on Bimetallic Nanoalloys with Site-Specific Precision. *J. Phys. Chem. Lett.* **2019**, *10*, 1852–1859.

(48) Jäger, M. O.; Morooka, E. V.; Federici Canova, F.; Himanen, L.; Foster, A. S. Machine learning hydrogen adsorption on nanoclusters through structural descriptors. *npj Comp. Mat.* **2018**, *4*, 37.

(49) Asara, G. G.; Paz-borbon, L. O.; Baletto, F. "Get in Touch and Keep in Contact": Interface Effect on the Oxygen Reduction Reaction (ORR) Activity for Supported PtNi Nanoparticles. *ACS Cat.* **2016**, *6*, 4388–4393.

(50) Liu, S.; White, M.; Liu, P. Mechanism of Oxygen Reduction Reaction on Pt(111) in Alkaline Solution: Importance of Chemisorbed Water on Surface. *J. Phys. Chem. C* **2016**, *120*, 15288–15298.

(51) Nørskov, J. K.; Abild-Pedersen, F.; Studt, F.; Bligaard, T. Density functional theory in surface chemistry and catalysis. *Proc. Nat. Ac. Sci.* **2011**, *108*, 937–943.

(52) Baletto, F. LoDiS: LoW-Dimensional Systems Molecular Dynamics. 2019; `https://github.com/orgs/kcl-tscm/teams/lodis`.

(53) Honeycutt, J. D.; Andersen, H. C. Molecular dynamics study of melting and freezing of small Lennard-Jones clusters. *J. Phys. Chem.* **1987**, *91*, 4950 – 4963.

(54) Baletto, F. Structural properties of sub-nanometer metallic clusters. *J. Phys. Cond. Matter* **2019**, *31*, 113001.

(55) Rossi, K.; Bartok-Pártay, L.; Csányi, G.; Baletto, F. Thermodynamics of CuPt nanoalloys. *Sci. Rep.* **2018**, *8*, 9150.

(56) Baletto, F.; Ferrando, R.; Fortunelli, A.; Montalenti, F.; Mottet, C. Crossover among

structural motifs in transition and noble-metal clusters. *J. Chem. Phys.* **2002**, *116*, 3856.

(57) Rossi, K.; Pavan, L.; Soon, Y.; Baletto, F. The effect of size and composition on structural transitions in monometallic nanoparticles. *Eur. Phys. J. B* **2018**, *91*, 33.

(58) Leontyev, I.; Belenov, S.; Guterman, V.; Haghi-Ashtiani, P.; Shaganov, A.; Dkhil, B. Catalytic Activity of Carbon-Supported Pt Nanoelectrocatalysts. Why Reducing the Size of Pt Nanoparticles is Not Always Beneficial. *J. Phys. Chem. C* **2011**, *115*, 5429–5434.

(59) Snyder, J.; McCue, I.; Livi, K.; Erlebacher, J. Structure/Processing/Properties Relationships in Nanoporous Nanoparticles As Applied to Catalysis of the Cathodic Oxygen Reduction Reaction. *J. Am. Chem. Soc.* **2012**, *134*, 8633–8645.

(60) Xia, Y.; Xia, X.; Peng, H. C. Shape-Controlled Synthesis of Colloidal Metal Nanocrystals: Thermodynamic versus Kinetic Products. *J. Am. Chem. Soc.* **2015**, *137*, 7947–7966.

(61) Foster, D.; Pavloudis, T.; Kioseoglou, J.; Palmer, R. Atomic-resolution imaging of surface and core melting in individual size-selected Au nanoclusters on carbon. *Nat. Comm.* **2019**, *10*.

(62) Palmer, R. E.; Cai, R.; Vernieres, J. Synthesis without Solvents: The Cluster (Nanoparticle) Beam Route to Catalysts and Sensors. *Acc. Chem. Res.* **2018**, *51*, 2296–2304.

(63) Piseri, P.; Tafreshi, H. V.; Milani, P. Manipulation of nanoparticles in supersonic beams for the production of nanostructured materials. *Curr. Op. Sol. Sta. Mat. Sci.* **2004**, *8*, 195–202.

(64) Vajda, S.; White, M. G. Catalysis Applications of Size-Selected Cluster Deposition. *ACS Cat.* **2015**, *5*, 7152–7176.

(65) Li, M.; Zhao, Z.; Cheng, T.; Fortunelli, A.; Chen, C. Y.; Yu, R.; Zhang, Q.; Gu, L.; Merinov, B. V.; Lin, Z.; Zhu, E.; Yu, T.; Jia, Q.; Guo, J.; Zhang, L.; Goddard, W. A.; Huang, Y.; Duan, X. Ultrafine jagged platinum nanowires enable ultrahigh mass activity for the oxygen reduction reaction. *Sci.* **2016**, *354*, 1414–1419.

(66) Strasser, P.; Koh, S.; Yu, C. Voltammetric surface dealloying of Pt bimetallic nanoparticles: A novel synthetic method towards more efficient ORR electrocatalysts. *ECS Trans.* **2007**, *11*, 1.

(67) Spanos, I.; Dideriksen, K.; Kirkensgaard, J. J.; Jelavic, S.; Arenz, M. Structural disordering of de-alloyed Pt bimetallic nanocatalysts: The effect on oxygen reduction reaction activity and stability. *Phys. Chem. Chem. Phys.* **2015**, *17*, 28044–28053.

(68) Sun, B.; Barron, H.; Opletal, G.; Barnard, A. S. From Process to Properties: Correlating Synthesis Conditions and Structural Disorder of Platinum Nanocatalysts. *J. Phys. Chem. C* **2018**, *122*, 28085–28093.

Graphical TOC Entry

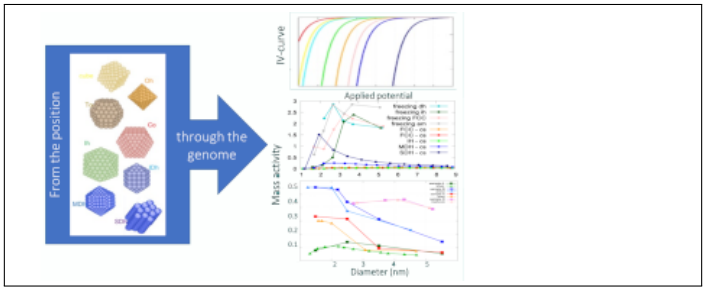

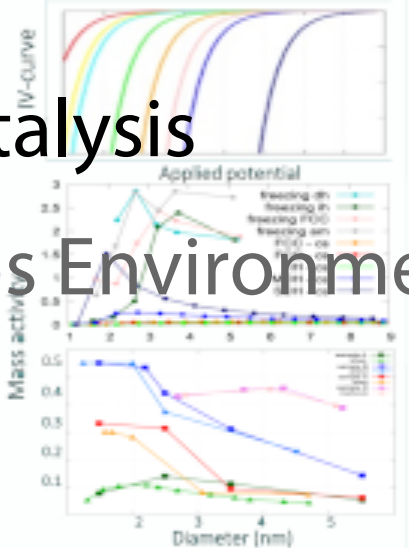

1

2